Magnetic interactions in $PdCrO_2$ and their effects on its magnetic structure

Manh Duc Le,[1,2] Seyyoung Jeon,[2,3] A. I. Kolesnikov,[4] D. J. Voneshen,[1] A. S. Gibbs,[1] Jun Sung Kim,[5,6] Jinwon Jeong,[7] Han-Jin Noh,[7] Changhwi Park,[3] Jaejun Yu,[3] T. G. Perring,[1] and Je-Geun Park[2,3]
[1]*ISIS Neutron and Muon Source, Rutherford Appleton Laboratory, Chilton, Didcot, OX11 0QX, United Kingdom*
[2]*IBS Research Center for Correlated Electron Systems, Seoul National University, Seoul 08826, Korea*
[3]*Department of Physics and Astronomy, Seoul National University, Seoul 08826, Korea*
[4]*Neutron Scattering Division, Oak Ridge National Laboratory, Oak Ridge, Tennessee 37831-6473, USA*
[5]*Department of Physics, Pohang University of Science and Technology, Pohang 37673, Korea*
[6]*Center for Artificial Low Dimensional Electronic Systems, Institute for Basic Science (IBS), Pohang 37673, Korea*
[7]*Department of Physics, Chonnam National University, Gwangju 61186, Korea*

(Received 16 April 2018; revised manuscript received 9 July 2018; published 31 July 2018)

We report a neutron scattering study of the metallic triangular lattice antiferromagnet $PdCrO_2$. Powder neutron diffraction measurements confirm that the crystalline space group symmetry remains $R\bar{3}m$ below T_N. This implies that magnetic interactions consistent with the crystal symmetry do not stabilize the noncoplanar magnetic structure, which was one of two structures previously proposed on the basis of single crystal neutron diffraction measurements. Inelastic neutron scattering measurements find two gaps at low energies, which can be explained as arising from a dipolar-type exchange interaction. This symmetric anisotropic interaction also stabilizes a magnetic structure very similar to the coplanar magnetic structure, which was also suggested by the single crystal diffraction study. The higher-energy magnon dispersion can be modelled by linear spin-wave theory with exchange interactions up to sixth nearest neighbors, but discrepancies remain which hint at additional effects unexplained by the linear theory.

DOI: 10.1103/PhysRevB.98.024429

I. INTRODUCTION

Geometric magnetic frustration, wherein the exchange interactions between spins on particular types of lattices cannot be simultaneously satisfied, can lead to novel ground states [1] and unusual excitations [2,3]. In the case of the triangular lattice, for example, a spin liquid ground state was famously predicted by Anderson [4] for $S = \frac{1}{2}$. Even for larger S, where a noncollinear 120° spin structure can provide a nondegenerate ground state to satisfy the frustration, effects such as magnon decays [5], magnon-phonon coupling [6,7], and multiferroicity have been observed. In addition, if the magnetic electrons are itinerant, complex chiral magnetic ordering can emerge due to Fermi surface nesting as a result of the triangular geometry [8]. Similar chiral structures are also obtained if the itinerant electrons, coupled by ferromagnetic double-exchange interactions, compete with antiferromagnetically (superexchange) coupled local moments [9].

One candidate for such a material is the metallic delafossite compound $PdCrO_2$, where Cr^{3+} ($S = \frac{3}{2}$) spins form triangular layers in the ab plane separated by O-Pd-O dumbbells, as shown in Fig. 1(a). The triangular chromium-oxide layers are insulating and host localized spins on the Cr ions, while the Pd d electrons are itinerant and form conducting layers sandwiched by the magnetic CrO_2 layers. In common with other metallic delafossites [10], the in-plane resistivity of $PdCrO_2$ is astonishingly low $\approx 9\ \mu\Omega$ cm at room temperature [11,12], which is of the same order of magnitude as elemental metallic conductors. This has motivated studies of its electronic structure, through quantum oscillations [11,13] and angle-resolved photoemission spectroscopy [14,15]. These works showed that the nonmagnetic Fermi surface is reconstructed into the magnetic Brillouin zone below the antiferromagnetic transition at $T_N = 37.5$ K, and suggest a strong coupling between the localized and conduction electrons.

One particularly interesting feature is the observation of an unusual anomalous Hall effect [16], in which the Hall coefficient is not proportional to the magnetization. This was attributed to a noncoplanar magnetic structure of the Cr spins which would allow a finite scalar spin chirality in the presence of a magnetic field [17]. The noncoplanar magnetic structure consists of spins in each triangular ab layers lying in a vertical plane whose orientation changes from layer to layer. The spin plane for each ab layer always includes the c-axis and makes an angle α with respect to the a-axis, as shown in Fig. 1(c). In the noncoplanar structure proposed by [17], there are two angles $\alpha_1 = 31°$ and $\alpha_2 = 44°$ for consecutive layers. However, the same single-crystal neutron diffraction study [17] found that this noncoplanar structure could barely be distinguished from a very similar *coplanar* structure, with a single $\alpha = 35°$ for all layers. This coplanar structure, however, has zero net scalar spin chirality and cannot explain the unconventional anomalous Hall effect.

To shed further light on this matter, we have used neutron scattering to elucidate the magnetic exchange interactions and constructed a spin Hamiltonian, which can be used to model and determine the most energetically favorable magnetic structure. This is supported by density functional theory calculations of the ground-state energy of the different magnetic structures. In addition, we were also motivated by the apparent strong coupling between the localized spins and conduction electrons

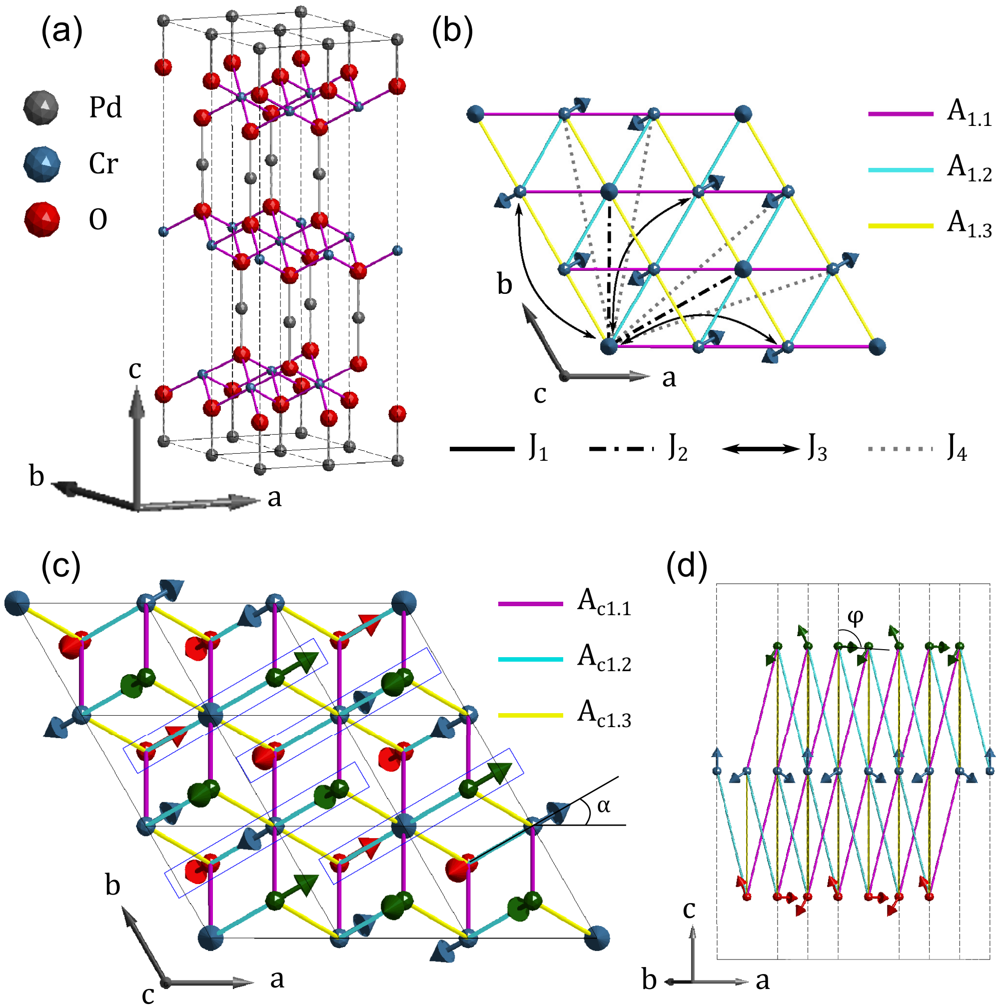

FIG. 1. The crystal and magnetic structure of $PdCrO_2$. (a) The crystal structure showing the Cr-O and Pd-O bonds. (b) A view of a single Cr layer with the in-plane magnetic interactions highlighted. Solid lines (shading-coded by the type of anisotropic dipolar interaction, labeled A_i) show nearest-neighbor couplings, while dash-dotted, arrowed, and lighter dotted lines show further neighbor interactions up to fourth nearest neighbor. Single-headed arrows indicate the spin moment direction for each Cr^{3+} ion, with some pointing along the c axis. Double-headed arrows indicate the exchange interactions. (c) The nearest interlayer interactions shading-coded by the type of dipolar interactions, and the angle α between the vertical spin plane and the a axis. The diagonal boxes show interlayer bonds whose exchange energy does not cancel, and indicate the preferred orientation of the spin plane as described in the text in Sec. III B 2. The ions in a particular layer are colored the same, with the lowest layer ($z = \frac{1}{6}$) in red, the middle layer ($z = \frac{1}{2}$) in blue and the top layer ($z = \frac{5}{6}$) in green. (d) shows a side view of the couplings in (c), the ϕ angle between equivalent spins in different layers, and also illustrates the staggered (alternating) chirality in different triangular layers, where the sense of the 120° rotation between adjacent spins change in different layers.

to look for how this would modify the exchange interactions compared to the localized case.

II. METHODS

A 22-g powder sample was synthesized through an ion-exchange reaction [18], and used in inelastic neutron scattering measurements on the Sequoia [19] (Spallation Neutron Source, Oak Ridge) and LET [20] (ISIS facility) spectrometers, while neutron powder diffraction measurements were performed on HRPD [21] (ISIS).

The Sequoia measurements used higher incident energies (8–120 meV) to observe the overall magnon dispersion over a wide temperature range from 5 to 200 K, while the LET measurements concentrated on the low energy gaps at 5 K using E_i from 1.8 to 7 meV. The inelastic data were reduced using the MANTID [22] program, and analyzed using the SPINW [23] linear spin-wave theory, and MCPHASE [24] mean-field modeling packages. The calculated spin-wave spectrum was convoluted with a Gaussian line shape whose width in energy transfer was obtained from an analytical calculation of the chopper opening times [25,26], and whose width in momentum transfer was obtained from the angular widths of the sample as seen from the moderator and detectors combined with the calculated divergence of the neutron guides at the incident energies used. We used the coplanar 120° magnetic structure

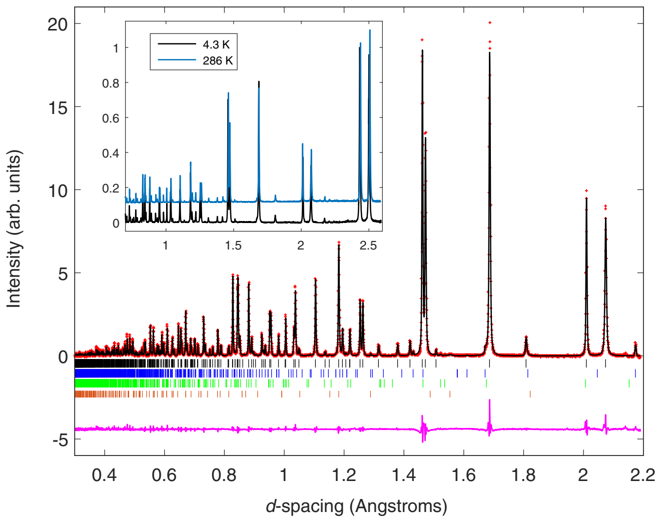

FIG. 2. The measured (red cross) and refined (black line) powder diffraction pattern of $PdCrO_2$ from the backscattering detectors of HRPD at 286 K. Ticks below the pattern indicate, in order from top to bottom, the positions of nuclear reflections of $PdCrO_2$ and the impurity phases Cr_2O_3 (0.63 wt%), PdO (0.84 wt%), and LiCl (0.13 wt%), respectively. The small peak at ≈ 2.14 Å is from the vanadium sample container. The inset shows the measured patterns at 286 and 4.3 K indicating that there is little change in the diffraction pattern below $T_N = 37.5$ K.

found in Sec. III B 2 for the spin-wave calculations, but also found that using either of the magnetic structures proposed in ref [17] produced negligible differences in the calculated convoluted spectra.

Diffraction patterns at 4.3 and 286 K were acquired on HRPD. Data from the backscattering detector banks in the time-of-flight range from 30–130 ms, and additionally 10–110 ms in the case of the 286 K data, were analyzed by the Rietveld method as implemented in the general structure analysis system (GSAS) [27] using the EXPGUI interface [28]. Density functional theory (DFT) calculations of $PdCrO_2$ were carried out to determine the stability of several magnetic structure models were carried out using the OPENMX code [29,30] within the LDA+U framework [31].

III. RESULTS

A. Neutron powder diffraction

Figure 2 shows the measured powder neutron diffraction data at 4.3 and 286 K. Very little difference was observed between the patterns measured above and below $T_N = 37.5$ K, as indicated by the inset. Rietveld refinements were carried out using the literature reported $R\bar{3}m$ and a distorted $C2/m$ crystal structure. The effects of anisotropic strain, after Stephens [32], and small[1] amounts of impurities were accounted for in the refinement. We found that at 286 K the $R\bar{3}m$ structure ($R_{\rm wp} = 3.34\%$, $\chi^2 = 6.38$ with isotropic displacement parameters) fitted better than the $C2/m$ structure ($R_{\rm wp} = 5.05\%$, $\chi^2 = 14.56$ with isotropic displacement parameters), while at 4.3 K, the two structures had similar R factors with the $R\bar{3}m$ structure very marginally smaller ($R_{\rm wp} = 2.46\%$, $\chi^2 = 9.47$ for $R\bar{3}m$ compared to $R_{\rm wp} = 2.48\%$, $\chi^2 = 9.63$ for $C2/m$, both with isotropic displacement parameters). We thus conclude that the space group of $PdCrO_2$ remains $R\bar{3}m$ below T_N, and that no symmetry lowering distortions could be observed. The refined parameters are given in Table I.

TABLE I. Anisotropic displacement parameters of $PdCrO_2$ in units of (100 Å^2) obtained from refinement of powder neutron diffraction data at room temperature, using the data from both the 10 to 110 ms and 30 to 130 ms time-of-flight windows. The space group is $R\bar{3}m$, with lattice parameters $a = 2.922692(15)$ Å and $c = 18.08691(11)$ Å. The Pd atoms are at the $3a$ Wyckoff sites (0, 0, 0), the Cr atoms occupy the $3b$ sites (0, 0, 0.5), and the O atoms the $6c$ sites (0, 0, z) with $z = 0.110511(8)$. The weighted $R_{wp} = 3.07\%$, with $\chi^2 = 5.383$.

Atom	U_{11}	U_{22}	U_{33}	U_{12}	U_{13}	U_{23}
Pd	0.673(6)	0.673(6)	0.426(10)	0.3364(28)	0.0	0.0
Cr	0.483(8)	0.483(8)	0.498(14)	0.242(4)	0.0	0.0
O	0.586(4)	0.586(4)	0.469(7)	0.2933(21)	0.0	0.0

The $R\bar{3}m$ crystal structure imposes several strong constraints on the terms of the spin Hamiltonian. The first is that the exchange interactions must agree with the point group symmetry of the midpoint of the Cr-Cr bond (Wyckoff d or e sites, for intra- or interlayer interactions respectively, both having point group $2/m$ or C_{2h}). The second is that single-ion anisotropy terms must be invariant under the operations of the point group symmetry of the magnetic Cr sites (Wyckoff b site, point group $\bar{3}m$ or D_{3d}). The threefold rotation axis parallel to c of D_{3d} implies that the only allowed quadratic anisotropy term is the KS_z^2 term, which may produce either an easy-axis along the c axis ($K < 0$) or an easy-plane perpendicular to the c axis ($K > 0$). An easy-axis single-ion anisotropy would favor a spin plane which includes the c axis as reported in [17], but the azimuth angle of the plane, α, would still be undetermined, as the ground-state magnetic energy for all α would be degenerate.

In the context of the proposed noncoplanar structure of $PdCrO_2$, however, the first point is more important, as the Wyckoff d and e sites, midpoints of all Cr-Cr pairs, are centers of symmetry. This implies that Dzyaloshinskii-Moriya (DM) interactions are forbidden [33] for all pairs of Cr spins. Since the alternating rotations of α in consecutive ab layers in the noncoplanar magnetic structure proposed by Ref. [17] may only be stabilized by an interlayer DM interaction, this constraint implies that the noncoplanar structure cannot be realized. This is in agreement with DFT calculations, which show that the coplanar magnetic structure has the lowest electronic ground-state energy, as explained in more detail in Sec. III C. Nonetheless, we cannot rule out the possibility that there exist very small distortions that cannot be detected by the current experiments and which break the inversion symmetry of the system and hence allow a DM interaction. Indeed, we note that any vertical 120° magnetic structure in this lattice breaks inversion symmetry, and will discuss these issues in greater detail in the conclusions.

[1]The impurities in our samples were determined to be PdO (0.84 wt%), Cr_2O_3 (0.63 wt%), and LiCl (0.13 wt%).

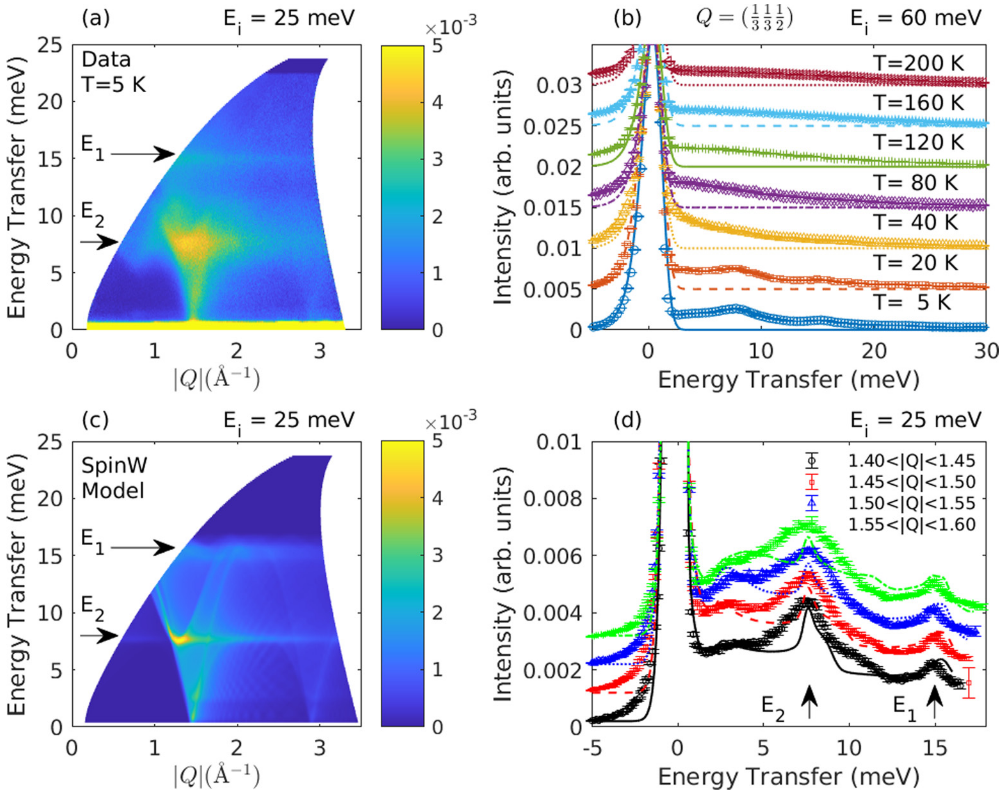

FIG. 3. Measured powder-averaged magnon spectra (a) from Sequoia with $E_i = 25$ meV, compared with (c) calculated spectra using SpinW. (b) and (d) Constant momentum transfer cuts around the magnetic Bragg peak at $Q = (\frac{1}{3}\frac{1}{3}\frac{1}{2})$ with (b) $E_i = 60$ meV, integrated over the range $1.4 < |Q| < 1.6\,\AA^{-1}$ and (d) $E_i = 25$ meV. Lines in (b) show the fitted elastic scattering of the 5 K data set, scaled to fit the elastic intensities of the other data sets, to emphasize the extensive low-energy inelastic scattering which persists to the highest temperatures measured. Lines in (d) are the sum of the fitted elastic peak and resolution convoluted calculations from linear spin-wave theory. In both (b) and (d), a peak shape defined by the convolution of an Ikeda-Carpenter and a pseudo-Voigt function was used to fit the elastic line.

B. Powder inelastic neutron scattering

Figure 3 shows the high-energy part of magnon spectrum obtained using the Sequoia spectrometer. Panels (a) and (d) show the data measured at 5 K with $E_i = 25$ meV as a 2D intensity map (a) and as cuts (d) along neutron energy transfer at constant $|Q|$ around the antiferromagnetic ordering wave vector $(\frac{1}{3}\frac{1}{3}\frac{1}{2})$ at $|Q| = 1.5\,\AA$. Two peaks at $E_1 = 15.4$ meV and $E_2 = 7.7$ meV are seen. Their momentum dependence follows the magnetic form factor of Cr^{3+} and we attribute them to van Hove singularities corresponding to the maxima of two different branches of the magnon dispersion. Panel (b) shows data measured at $E_i = 60$ meV as a function of temperature. The two magnon peaks disappear above $T_N = 37.5$ K but a significant amount of low-energy inelastic scattering remains up to 200 K, indicating that magnetic fluctuations persist up to at least $5T_N$. These are likely to be associated with correlations within the triangular *ab* layers where the exchange interactions are strong, while the magnetic ordering results from the weaker interlayer exchange interaction coupling each layer. This is consistent with the large difference between the Curie-Weiss temperature ($\theta_{\mathrm{CW}} \approx 500$ K [34]) compared to T_N in this compound, indicating that the interlayer interactions that are responsible for the Nèel ordering are significantly smaller than other interactions in the system.

Figure 4 shows the data measured with $E_i = 7$ and 3 meV using the LET spectrometer. Two clear energy edges, at $E_3 = 2.2$ and $E_4 = 0.4$ meV, can be seen in the energy cuts, which are likely to be from energy gaps caused by the magnetic anisotropy. However, as noted in Sec. III A, only the KS_z^2 single-ion anisotropy term is allowed by the crystalline symmetry of $PdCrO_2$, and this term only results in a single anisotropy energy gap, rather than the two observed edges E_3 and E_4. This suggests that an additional interaction must be included, and this, together with its effect on the magnetic structure, is considered in Sec. III B 2. However, we will first discuss how the Heisenberg exchange interactions can be obtained from the high-energy data.

1. High-energy spectrum

The dominant magnetic interaction between Cr^{3+} ions, with $S = \frac{3}{2}$, is expected to be the superexchange, which generally results in a Heisenberg Hamiltonian:

$$\mathcal{H}^{\mathrm{Heisenberg}} = \sum_{ij} J_{ij}\mathbf{S}_i \cdot \mathbf{S}_j + \sum_i K\left(S_z^{(i)}\right)^2, \tag{1}$$

where the exchange interactions J_{ij} between ion pairs i and j up to sixth-nearest-neighbor are considered in this work, and K is the single-ion anisotropy constant. The peak energies $E_1 = 15.4$ meV and $E_2 = 7.7$ meV may be modelled by the above spin Hamiltonian in linear spin-wave theory, and

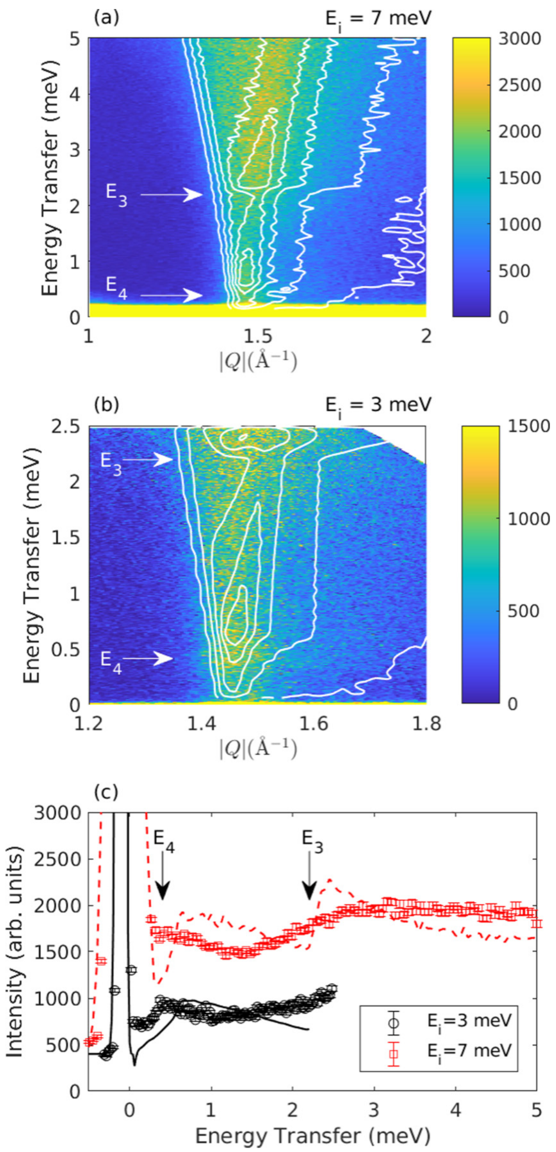

FIG. 4. Measured powder-averaged magnon spectra from LET with (a) $E_i = 7$ and (b) 3 meV, compared with calculated spectra using SpinW (white contour lines). (c) Constant $|Q|$ cuts integrating over the range [1.4, 1.5] Å^{-1} of the $E_i = 7$ meV (red squares) and $E_i = 3$ meV (black circles) data with linear spin-wave theory calculations (solid and dashed lines) for the model discussed in the text.

correspond to the energy of modes at the magnetic Brillouin zone edges where next-nearest neighbor spins (which are ferromagnetically aligned) precess either in-phase (E_2) or in antiphase (E_1). Note that for both modes, nearest neighbor spins (aligned at 120° with respect to each other) precess in antiphase. This means that for the E_2 mode one third of next-nearest spins cannot be satisfied and thus remain stationary. That is, they cannot simultaneously precess in-phase with their next-nearest neighbors while in antiphase with their nearest neighbors. Thus a spin-wave model with only nearest-neighbor interactions implies a ratio $E_1 = 1.5E_2$ [2] because only two thirds as many spins contribute. The actual value of E_1 is determined by $E_1 \approx 5J_1$.

That we observe a ratio closer to $E_1 \approx 2E_2$ thus requires nonzero further neighbor interactions. A ferromagnetic next-nearest neighbor interaction, J_2, pushes E_2 higher in energy relative to E_1, because it favors the in-phase precession of next-nearest neighbor spins and thus allows more than two thirds of spins to participate in the E_2 mode. A ferromagnetic third-nearest-neighbor interaction, J_3, on the other hand, acts in the opposite way to decrease the energy of E_2 with respect to E_1. This suggests that to match the observed ratio of the peak energies $E_1/E_2 \approx 2$, an antiferromagnetic $J_2 > 0$ or a ferromagnetic $J_3 < 0$ is needed. An in-plane fourth-nearest-neighbor interaction, J_4, on the other hand, does not change the ratio E_1/E_2 but serves to scale the overall bandwidth of the magnon excitations in a similar way to J_1, so we will not consider it or further neighbor interactions in the following analysis.

Setting either J_2 or J_3 to zero would yield unique values of the two remaining in-plane exchange interactions from the two observed energies E_1 and E_2. However, previous analyses [35,36] of data for $CuCrO_2$, which also adopts the delafossite structure and has a similar magnetic structure, have retained up to third nearest neighbor interactions, which were determined to be still significant ($J_2/J_1 \approx 18\%$ and $J_3/J_1 \approx 3\%$ [36]). Furthermore, for two nonzero interactions (either J_1 and J_2 or J_1 and J_3), the E_1 and E_2 peak intensities are calculated to be approximately equal, or with the E_1 peak slightly more intense than the E_2 peak, in clear contrast to the data, where the ratio of the peaks is $I_2/I_1 \approx 2$. This can be rectified by increasing $|J_2|$ as this favors the in-phase precession of the E_2 mode as noted above.

Using these two constraints, $E_1/E_2 = 2$ and $I_2/I_1 = 2$, and the absolute energies of the peaks E_1 and E_2, we obtained the intralayer exchange interactions J_1, J_2, and J_3 listed in Table II. These exchange constants give a mean-field Curie-Weiss temperature $\theta_{\mathrm{CW}}^{\mathrm{mean-field}} = -725$ K, which somewhat

TABLE II. Spin wave exchange parameters fitted to data in meV. Positive values indicate antiferromagnetic exchange. Also shown is the reduced χ^2 calculated from the cuts shown in Figs. 3 and 4, and the mean-field calculated Néel and Curie-Weiss temperatures from the stated exchange constants (T_N is calculated from only the interlayer interactions, while θ_{CW} is calculated from all exchanges). For comparison, the measured values are $T_N = 37.5$ K and $\theta_{\mathrm{CW}} = -500$ K [34].

		Bond dist (Å)
J_1 (meV)	6	2.9
J_2 (meV)	1.2	5.1
J_3 (meV)	0.6	5.8
J_{c1} (meV)	0.3	6.2
J_{c2} (meV)	0.13	6.9
J_{c3} (meV)	0.048	7.5
K (meV)	−0.02	
χ^2_{red}	43.5	
T_N^{MF} (K)	39	
$\theta_{\mathrm{CW}}^{\mathrm{MF}}$ (K)	−725	

[2]The E_1/E_2 ratio also has a weak quadratic dependence on the single-ion anisotropy K, which is not considered here.

overestimates the observed $\theta_{CW}^{measured} = -500$ K [34]. This is because the $I_2/I_1 = 2$ ratio implies a large $|J_2|$, which in turn demands a larger $|J_1|$ and a larger $|J_3|$ of the same sign as J_2 to keep the $E_1/E_2 = 2$ ratio, as J_3 acts opposite to J_2 with respect to the E_1/E_2 ratio as described above. As can be seen in Fig. 3, however, the width of peak E_2 at 7.7 meV is not resolution limited and it has a low-energy shoulder which cannot be fitted by our linear spin-wave theory model, regardless of the number of parameters included. There is thus some uncertainty in the integrated intensity I_2 and hence in the ratio I_2/I_1, which may well be smaller than we have used here, thus resulting in an overall reduction of the estimates of the exchange interactions. In any case, the exchange interactions given here should be considered an approximate estimate, and a more detailed single-crystal study of the magnon dispersion will be needed to obtain more accurate values. Nonetheless, we note that the exchange interactions obtained here are consistent with $PdCrO_2$ having a coplanar 120° magnetic structure according to the theoretical phase diagrams of Messio *et al.* [37]. On this phase diagram, a larger J_2 or smaller (or ferromagnetic) J_3 would stabilize a noncoplanar magnetic structure, but this structure would have magnetic Bragg reflections at $(\frac{1}{2}00)$ and equivalent points, in contrast to observations.

Whilst the intralayer interactions determine the energies of the two peaks seen in the constant $|Q|$ cuts, the main effect of the interlayer exchange is to broaden the peak widths by lifting the degeneracy of the magnon modes at the zone boundary. However, large values of this interlayer interaction would stabilize an incommensurate magnetic structure [35], in contrast to observations which showed that the propagation vector, $q = (\frac{1}{3}\frac{1}{3}\frac{1}{2})$, is commensurate. In addition, the long-range 3D Néel order depends strongly on the interlayer interaction, such that they are the main determinant of T_N. We have thus used mean-field calculations of T_N, the requirement that the spin-wave eigenvalues at the Γ point should be real (which would otherwise indicate an incommensurate structure is more favorable), and the width of the $E_1 = 15.4$ meV peak to determine the three nearest-neighbor interlayer exchange interactions J_{c1}, J_{c2}, and J_{c3} as shown in Table II. As with the intralayer interaction, however, there is a degree of uncertainty in these parameters because the major feature of the data sensitive to them, the widths of the magnon peaks, may also have contributions from other processes, such as magnon decay. A single crystal measurement of the dispersion along Q_L is thus needed to accurately determine these parameters.

2. Low-energy spectrum

As noted in Sec. III B, we observe two anisotropy gaps, $E_3 = 2.2$ meV and $E_4 = 0.4$ meV, while only one single-ion anisotropy term yielding one anisotropy gap is permitted by the D_{3d} point symmetry of the Cr site. Thus in addition to the Heisenberg term (1), we turn to an anisotropic exchange interaction as the mechanism behind the second gap. However, the measured magnetic susceptibility along the c axis and in the ab plane is very similar [34], which implies that any anisotropic exchange interaction is small. One possible interaction is the dipolar coupling, which may arise classically from interactions between local Cr spin moments, or from a modification of the direct or superexchange interactions by the spin-orbit coupling. This latter case is often referred as a *pseudodipolar* interaction, in contrast to the classical mechanism, and has a coupling strength which scales with the square of the spin-orbit coupling constant [33,38,39]. The dipolar interaction is symmetric, and thus is not forbidden by the C_{2h} Cr-Cr bond symmetry, in contrast to the Dzyaloshinskii-Moriya interaction which is antisymmetric and does not satisfy the bond symmetry.

The form of the dipolar interaction is given by

$$\mathcal{H}_{ij}^{\text{dipolar}} = -\frac{\mu_0 g^2 \mu_B^2}{4\pi} \frac{3(\mathbf{S}_i \cdot \hat{\mathbf{r}}_{ij})(\mathbf{S}_j \cdot \hat{\mathbf{r}}_{ij}) - \mathbf{S}_i \cdot \mathbf{S}_j}{r_{ij}^3} \quad , \tag{2}$$

which may also be expressed as $\mathcal{H}_{ij}^{\text{dip}} = \mathbf{S}_i \overline{\overline{\mathbf{A}}}_{ij} \mathbf{S}_j$ where $\overline{\overline{\mathbf{A}}}_{ij} = -\frac{\mu_0 g^2 \mu_B^2}{4\pi r_{ij}^3}(3\hat{\mathbf{r}}_{ij}\hat{\mathbf{r}}_{ij}^\top - \delta_{ij})$. The $\mathbf{S}_i \cdot \hat{\mathbf{r}}_{ij}$ and $\mathbf{S}_j \cdot \hat{\mathbf{r}}_{ij}$ terms couple only the components of the spins along the bond direction $\hat{\mathbf{r}}_{ij}$, which makes the dipolar (or pseudodipolar) interaction bond- and magnetic-structure dependent. In addition, these terms also result in the $\mathbf{r}_{ij}$ direction being a local easy direction. For $PdCrO_2$, there are three inequivalent bonds for the nearest-neighbor intra- and interplane interactions, which are shown in Figs. 1(b) and 1(c).

Let us consider first the nearest neighbors within a triangular ab plane. Figure 1(b) shows that each type of dipolar bond (denoted by different colored solid lines) connects a spin to neighboring spins, which are rotated at +120° and −120° with respect to it (note that as the figure shows the projection onto the ab plane, the spins appear to be aligned antiparallel). This means that the $(\mathbf{S}_i \cdot \hat{\mathbf{r}}_1)(\mathbf{S}_j \cdot \hat{\mathbf{r}}_1)$ term (for nearest neighbors linked by $\mathbf{r}_1$) cancels for each type of bond, so that no particular in-plane spin direction is favored by the nearest-neighbor dipolar interaction. However, since $\hat{\mathbf{r}}_1$ has no z component, this term also has no z component, which means that there is a net Ising-like $-S_i^z S_j^z$ easy-axis anisotropy from the final $-\mathbf{S}_i \cdot \mathbf{S}_j$ term in equation (2). The cancellation of the in-plane exchange components leaving a net c-axis anisotropy also holds true for the other in-plane dipolar interactions. This net c-axis anisotropy provides one of the two observed spin anisotropy energy gaps.

In addition, the local easy axis defined by each $\mathbf{r}_{ij}$ bond direction serves to lift the degeneracy of the spin waves with precession axes that include a component in the ab plane, and yields the required second energy gap observed in the data. Using the combined Hamiltonian $\mathcal{H}^{\text{Heisenberg}} + \mathcal{H}^{\text{dipolar}}$ and values of $\overline{\overline{A}}_{1,n}$ obtained from the classical dipolar interaction ($|\overline{\overline{A}}_{1,n}| \approx 0.02$ meV), we found splittings of $E_3^{\text{calc}} \approx 1.6$ meV and $E_4^{\text{calc}} \approx 0.5$ meV. Thus, the calculated E_4 is slightly higher than that measured, as illustrated in Fig. 4. The larger energy gap E_3 is from the Ising-like c-axis anisotropy term, which acts on all spins, while the smaller energy gap E_4 is from the in-plane dipolar anisotropy where each type of dipolar interaction acts only on one third of spins. In order to better fit the observed $E_3 = 2.2$ meV, a small easy axis single-ion anisotropy term $K = -0.02$ meV needs to be added. The lower observed value of $E_4 = 0.4$ meV compared to $E_4^{\text{calc}} \approx 0.5$ meV may be due to screening of the moments.

Because of the rhombohedral symmetry, successive triangular layers along the c axis are offset by $\frac{1}{3}$ of a unit cell in the [110] direction, which means that the symmetry of the interlayer dipolar interactions is different to that of the in-plane interactions. The three inequivalent bonds are shown in Fig. 1(c) by different colored lines. Unlike for the in-plane interactions, the nearest neighbor spins connected by a given dipolar bond do not necessarily form pairs whose energy cancels. Instead, as highlighted by the light blue rectangles in the figure, one set of dipolar bonds will connect next-neighbor (interlayer) spins which are parallel. The energy of these bonds will be lower than the other two bonds, so that its preferred direction (along the bond direction) is also the globally preferred spin direction.

In Fig. 1, we chose one particular stacking of the *ab*-layer 120° magnetic structure which favors the blue $A_{c1,2}$ bonds and hence $\alpha = 30^\circ$. This choice was made for consistency with the single crystal diffraction work of Ref. [17]. However, there are other stacking arrangements that would favor either of the other two types of bonds, and hence either $\alpha = 90^\circ$ or $\alpha = 150^\circ$, which are energetically equivalent to the case we have illustrated. Thus, in a real crystal, there would be different domains where the easy plane is in these other directions. Finally, we note that the planes defined by $\alpha = 30^\circ$, 90°, and 150° are the vertical mirror planes of the $R\bar{3}m$ structure. Choosing one of these mirror planes to be the spin plane breaks the threefold symmetry of the crystalline structure so the symmetry of the magnetic structure becomes $C2'$. This symmetry breaking arises from the combination of the in-plane magnetic structure, which has a threefold periodicity, and the interlayer dipolar interaction, which has a twofold periodicity but depends on the relative orientations of the spins. Thus, while each interaction individually obeys the crystal symmetry, together they act to break it in the magnetic structure, without necessarily requiring a symmetry breaking crystal distortion.

The angle $\alpha = 30^\circ$ is close to that reported ($\alpha = 35^\circ$) for the coplanar structure of $PdCrO_2$ [17]. Moreover, equivalent values have also been reported in similar Cr-based delafossite compounds, which have vertical 120° spin structures. In particular, $CuCrO_2$ has $\alpha = 150^\circ$ [40] (spins in the $[1\bar{1}0]$-$[001]$ plane, and equivalent to $\alpha = 30^\circ$), and $LiCrO_2$ has $\alpha = 158^\circ$ [41] (equivalent to $\alpha = 38^\circ$). Thus both these cases can also be explained by a dipolar interaction.

In addition to favoring a particular spin plane orientation α, the interlayer dipolar interaction also forces the spins in alternating planes to be rotated by an additional angle, denoted ϕ, around the plane normal. Unlike for α, where the preferred angle is determined by geometry, ϕ is very sensitive to the relative magnitude of the off- and on-diagonal components of the dipolar interaction tensor. Whilst the geometry will fix a particular value for this ratio, and hence ϕ, for a set of neighboring spins at a particular distance, this will be different for a set of further neighbors. Thus we observed that varying the range of the dipolar interaction in the calculations can change ϕ drastically across the full range of angles. This implies that ϕ will be particularly sensitive to defects or stacking faults in the material, which will modify the dipolar interaction at longer ranges, and the physically observed ϕ cannot be predicted with any degree of confidence from the dipolar model.

The energy splittings between the spin-wave branches at Γ vary approximately as $\sqrt{|\overline{\overline{A}}_{ij}|}$, so due to the $\frac{1}{r_{ij}^3}$ dependence of the dipolar interaction, one would expect that the additional splitting of the spin-wave branches caused by the interlayer interaction is $\approx \frac{1}{3}$ that of the nearest-neighbor intralayer interaction, since $r_1 = 2.9$ Å and $r_{c1} = 6.2$ Å. This serves to smear out the edges E_3 and E_4 but does not significantly shift their energies. However, because of the small magnitudes of the further neighbor dipolar interactions, this smearing is minimal. In particular, it cannot explain the relatively smooth edge seen in the data in Fig. 4(c) compared to the sharper calculated edge. The observed width of the edge is much broader than the instrument energy resolution, suggesting that it is caused by some other interaction which lifts the degeneracy of the magnon modes at the zone center thus giving a range of gap energies. Large interlayer interactions J_{cn} would have this result and can give better fit to this low-temperature data, but will also give a much broader $E_1 = 15.4$ meV peak in disagreement with the high-energy data.

Despite this, the close agreement between the α angles implied by the dipolar interaction with that measured strongly suggests that this interaction plays a large role in determining the magnetic structure of $PdCrO_2$. Moreover, the nearest neighbor dipolar interaction can also explain the presence of two energy edges in the low-energy magnetic excitation spectrum, whereas the symmetry allowed single-ion anisotropy term can only yield one energy gap. That the energies of the edges predicted by the nearest-neighbor classical dipolar interaction (1.6 and 0.5 meV) and those measured ($E_3 \approx 2$ meV and $E_4 \approx 0.4$ meV) agree relatively well also reinforces the importance of the dipolar interaction.

C. *Ab initio* calculations

To gain further insights into the magnetic structures of $PdCrO_2$, we perform DFT calculations using the OPENMX code [29–31] to obtain the total energies for a series of different noncollinear magnetic structures and determine the lowest energy structure. We adopt the LDA+U framework with an effective U parameter of $U = 3.7$ eV for the description of on-site Coulomb interactions for the Cr d orbitals. This value is consistent with the Materials Project database [42] and is close to the one used in the study of isostructural $LiCrO_2$ [43]. Certainly, the choice of U can affect the calculated total energies, but we confirmed that the relative energy differences among the spin configurations under consideration remain robust for the range of U values between 3 and 4 eV.

We investigate the energies of various spin configurations starting from the proposed noncoplanar magnetic structure with the angles: $\alpha_1 = 31^\circ$, $\alpha_2 = 44^\circ$, $\phi_1 = 17^\circ$, $\phi_2 = 16^\circ$, $\zeta_1 = +1$, and $\zeta_2 = -1$, as suggested in Ref. [17]. Here, the α_i angles define the vertical spin planes across the consecutive Cr layers, the ϕ_i angles stand for the relative phase of the spins within the plane, and ζ_i's represent the handedness, i.e., chirality, of the 120° rotation among neighboring spins within the same Cr *ab* layers. To examine the energetics near this noncoplanar spin configuration, for the sake of clarity, we first calculate total energies by varying α_2 with all the other angles fixed at the proposed values. Figure 5(a) illustrates the calculated total energies as a function of α_2 and shows its minimum close to $\alpha_2 = 31^\circ$, which is different from the proposed structure of Ref. [17]. Figure 5(b) confirms that $\alpha_2 = \alpha_1 = 31^\circ$ is the minimum for the fixed ϕ_1 and ϕ_2, albeit

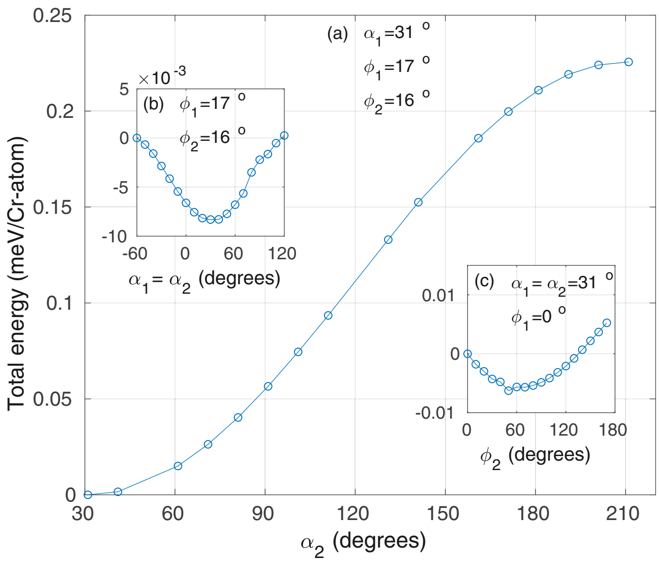

FIG. 5. DFT calculated total energy of different magnetic structures. (a) shows the variation between the coplanar (with $\alpha_2 = 31^\circ$) and noncoplanar (other values of α_2) with other angles fixed as described in the text. (b) shows the total energy as a function α for a coplanar structure and (c) shows the variation of the total energy with the difference between the ϕ angles of consecutive layers. In all cases, $\zeta_1 = +1$ and $\zeta_2 = -1$ applies, which means that the sense of the 120° rotation between neighboring spins in the same layer alternates in consecutive layers, which is the staggered chirality case described in the text.

the variation in the total energies is very small, of the order $10\,\mu$eV/Cr-atom. Although the magnetic ordering with $\alpha_1 = \alpha_2$ is coplanar, there are still possibilities of having variations of ϕ_i angles within the coplanar plane. Hence we have examined total energies with varying the ϕ_i angles and found that the energy dependence on ϕ_i is extremely small at the order of dozens of μeV/Cr-atom but its relative difference is still meaningful within the computational precision. As shown in Fig. 5(c), the energy curve for given values of $\alpha_2 = \alpha_1 = 31^\circ$ and $\phi_1 = 0^\circ$ has a minimum at $\phi_2 \approx 60^\circ$.[3] Thus, from DFT calculations, we conclude that the coplanar structure (with $\alpha_2 = \alpha_1 = 31^\circ$) is energetically favored over the noncoplanar ordering. Further, it is interesting to note that there is a large energy difference between the $\alpha_2 = \alpha_1$ and $|\alpha_2 - \alpha_1| = 180^\circ$ configurations. The configuration with $|\alpha_2 - \alpha_1| = 180^\circ$ is also coplanar but has the same chirality of $\zeta_1 = \zeta_2 + 1$ between the alternating layers, while the $\alpha_2 = \alpha_1$ configuration has the staggered chirality of $\zeta_1 = +1$ and $\zeta_2 = -1$. The configuration of $\alpha_2 = \alpha_1$ is indeed consistent with the observed staggered chirality in experiments [17]. However, this contrasts with the classical spin energy calculations used in Sec. III B 2 with the dipolar interaction, where both straight ($\zeta_1 = \zeta_2 = +1$) and staggered ($\zeta_1 = +1, \zeta_2 = -1$) chirality yields the same energy. The stability of the staggered chirality may reflect the influence of the conduction electrons on the magnetic ordering, which is ignored by the dipolar calculations.

IV. DISCUSSIONS

We have carried out a neutron scattering investigation of the metallic triangular lattice antiferromagnet $PdCrO_2$. Neutron powder diffraction shows no evidence of symmetry lowering in the magnetically ordered phase. This implies that the antisymmetric anisotropic Dzyaloshinskii-Moriya interaction is forbidden for all pairs of Cr spins, which means that the noncoplanar magnetic structure posited by Ref. [17] cannot be stabilized by a spin Hamiltonian consistent with the symmetry of the space group of $PdCrO_2$. On the other hand, the allowed *symmetric* anisotropic dipolar interaction was found to adequately explain the measured low-energy inelastic neutron spectrum and also explains the observed easy spin plane, which includes the c axis. Nonetheless, we note that this coplanar magnetic structure (or, indeed, *any* 120° magnetic structure with a vertical spin plane) has space group $P2'$ and thus itself breaks inversion symmetry. This may, in turn lead to a nonzero DM interaction and a noncoplanar magnetic structure. It is uncertain whether the magnitude of such a DM interaction may produce the reported noncoplanar structure, with spin planes canted by 13° with respect to each other, however. In any case, such an interaction would produce splittings of the magnon modes which would be too small to be experimentally measured.

The nonlinear field dependence of the Hall resistivity observed in Ref. [16] was attributed to an unconventional anomalous Hall effect arising from the effect of a noncoplanar magnetic structure on the Berry curvature. However, a recent theoretical work [44] suggests that a noncoplanar structure is only a prerequisite for the unconventional anomalous Hall effect in the absence of spin-orbit coupling. Reference [44] showed that, as the Berry curvature is not affected by translational symmetry, only the magnetic point symmetry needs to be considered. In particular, it noted that if there is a twofold rotation axis through the magnetic ion, then only the component of the tensor which is parallel to this axis will be nonzero. The coplanar magnetic structure stabilized by the dipolar interactions, where the vertical spin plane is coincident with a mirror plane of the structural $R\bar{3}m$ space group (with $\alpha = 30$, 90, or 150°), adopts the $C2'$ magnetic space group, which has a twofold rotation axis perpendicular to the spin plane (parallel to the a, b, or [110] axes), passing through the Cr sites. Thus, depending on the magnetic domain, either σ_{xz} or σ_{yz} is nonzero. This contradicts the experimental findings of Ref. [16], where a nonzero σ_{xy} was measured.

This suggests a number of possibilities to explain the observed Hall resistivity. First, there may be some other anisotropy which modifies the magnetic structure of $PdCrO_2$ so as to move the spin plane off an $R\bar{3}m$ mirror plane, and hence break the twofold rotation symmetry allowing a nonzero σ_{xy}, as measured. Alternatively there could be a small noncoplanarity, since our *ab initio* calculations show that while the coplanar structure is energetically favorable, small deviations from this only marginally raise the total energy (by around $1\,\mu$eV/Cr for $\approx 10^\circ$), as does a small shift of the spin plane off the $R\bar{3}m$ mirror planes. Furthermore, the mechanism by which the dipolar interaction stabilizes the coplanar structure depends on the fact

[3]The ϕ angle in Sec. III B 2 is actually the absolute difference between the ϕ of consecutive layers and effectively corresponds to ϕ_2 in Fig. 5(c) with $\phi_1 = 0^\circ$.

that a Cr layer above a particular layer is exactly equivalent to that below. So, it is possible that small lattice imperfections, such as vacancies or stacking faults, may introduce an additional single-ion anisotropy or modify the dipolar interaction so that in reality $PdCrO_2$ would not adopt the idealized magnetic structure favored by the model Hamiltonian.

Another possibility is that the observed nonlinear field dependence of the Hall resistivity at low temperatures is the result of the Fermi surface reconstruction due to the $\sqrt{3} \times \sqrt{3}$ magnetic ordering and tunneling between the reconstructed bands as suggested in Ref. [13]. In this case, a noncoplanar magnetic structure (nonzero scalar spin chirality) is not needed at zero magnetic field. Instead, the complex behavior of the Hall conductivity at low magnetic fields may be qualitatively explained by competition between the transport in different hole and electron bands, and tunneling between them. The true unconventional anomalous Hall effect in this scenario only manifests at high magnetic fields where the spin moments may cant out of plane to give a nonzero scalar spin chirality. In many respects, this is the most attractive possibility and would accord well with the neutron diffraction and inelastic data, which suggests that the magnetic structure remains coplanar. It may also offer a more robust explanation of the observed nonlinear field dependence of the Hall resistivity, than relying on a small noncoplanarity of the spin planes in alternating *ab* layers. However, numerical calculations of the Hall conductivity as a function of the noncoplanarity would be needed to properly decide between these explanations.

Finally, we turn to the high-energy magnon excitations. The exchange parameters listed in Table II were deduced entirely from two peaks in the inelastic neutron spectrum. While they account for gross features of the data, there remain many discrepancies. These are, principally, the extra scattering below the E_2 peak around 6 meV, and an apparent minimum in the dispersion at the same energy around $|Q| \approx 0.8$ Å^{-1}. It is important to note here that we have assumed that the single-ion anisotropy is small ($|K| \ll 0.1$ meV) throughout our analysis. This is in contrast to the published spin Hamiltonian for isostructural $CuCrO_2$ [35,36], where $K \approx 0.5$ meV was reported. In fact, such a large K set of parameters also fits the high-energy $PdCrO_2$ data, and would explain better the low-energy shoulder on the E_2 peak around 6 meV. However, this is because the large K pushes the E_3 and E_4 anisotropy gaps high in energy to near E_2, so the two low-energy gaps we observed could not be explained by this large K model. Instead, perhaps recent work on the magnon-phonon coupling in $LiCrO_2$ [43] and $CuCrO_2$ [45] where a low $|Q|$ dispersion minimum similar to that observed here was seen could explain the unexpectedly large broadening of the magnons at E_1 and E_2. However, due to the powder averaging of the data, and lack of detailed information on the phonon dispersion, we could not model such a magnon-phonon coupling for $PdCrO_2$.

Nonetheless, the similarities of the magnetic excitations and magnetic structures of these compounds strongly suggest a uniform mechanism behind their behavior. This similarity, despite $PdCrO_2$ being a metal, and $CuCrO_2$ and $LiCrO_2$ being insulators, suggests that the effect of the conduction electrons on the local chromium moments is subtle. Teasing out such effects will thus require further investigations with a single crystal using neutron and x-ray scattering measurements.

ACKNOWLEDGMENTS

The authors thank Young-June Kim for insightful discussions. The work at the Institute for Basic Science (IBS) CCES was supported by the research program of Institute for Basic Science (IBS-R009-G1). J.Y., J.J., and H.J.N. acknowledges the support by the National Research Foundation of Korea (NRF), no. 2012M2B2A4029607 (J.J. and H.J.N.) and no. 2017R1A2B4007100 (J.Y.). This research used resources at the Spallation Neutron Source, a DOE Office of Science User Facility operated by the Oak Ridge National Laboratory (ORNL). Experiments at the ISIS Neutron and Muon Source were supported by a beamtime allocation from the Science and Technology Facilities Council.

[1] J. S. Gardner, M. J. P. Gingras, and J. E. Greedan, Rev. Mod. Phys. **82**, 53 (2010).
[2] D. J. P. Morris, D. A. Tennant, S. A. Grigera, B. Klemke, C. Castelnovo, R. Moessner, C. Czternasty, M. Meissner, K. C. Rule, J.-U. Hoffmann, K. Kiefer, S. Gerischer, D. Slobinsky, and R. S. Perry, Science **326**, 411 (2009).
[3] S. T. Bramwell, S. R. Giblin, S. Calder, R. Aldus, D. Prabhakaran, and T. Fennell, Nature (London) **461**, 956 (2009).
[4] P. Anderson, Mater. Res. Bull. **8**, 153 (1973).
[5] M. E. Zhitomirsky and A. L. Chernyshev, Rev. Mod. Phys. **85**, 219 (2013).
[6] J. Oh, M. D. Le, J. Jeong, J.-h Lee, H. Woo, W.-Y. Song, T. G. Perring, W. J. L. Buyers, S.-W. Cheong, and J.-G. Park, Phys. Rev. Lett. **111**, 257202 (2013).
[7] J. Oh, M. D. Le, H.-H. Nahm, H. Sim, J. Jeong, T. G. Perring, H. Woo, K. Nakajima, S. Ohira-Kawamura, Z. Yamani, Y. Yoshida, H. Eisaki, S.-W. Cheong, and J.-G. Park, Nat. Commun. **7**, 13146 (2016).
[8] I. Martin and C. D. Batista, Phys. Rev. Lett. **101**, 156402 (2008).
[9] S. Kumar and J. van den Brink, Phys. Rev. Lett. **105**, 216405 (2010).
[10] A. P. Mackenzie, Rep. Prog. Phys. **80**, 032501 (2017).
[11] C. W. Hicks, A. S. Gibbs, L. Zhao, P. Kushwaha, H. Borrmann, A. P. Mackenzie, H. Takatsu, S. Yonezawa, Y. Maeno, and E. A. Yelland, Phys. Rev. B **92**, 014425 (2015).
[12] H. Takatsu, S. Yonezawa, C. Michioka, K. Yoshimura, and Y. Maeno, J. Phys.: Conf. Ser. **200**, 012198 (2010).
[13] J. M. Ok, Y. J. Jo, K. Kim, T. Shishidou, E. S. Choi, H.-J. Noh, T. Oguchi, B. I. Min, and J. S. Kim, Phys. Rev. Lett. **111**, 176405 (2013).
[14] J. A. Sobota, K. Kim, H. Takatsu, M. Hashimoto, S.-K. Mo, Z. Hussain, T. Oguchi, T. Shishidou, Y. Maeno, B. I. Min, and Z.-X. Shen, Phys. Rev. B **88**, 125109 (2013).
[15] H.-J. Noh, J. Jeong, B. Chang, D. Jeong, H. S. Moon, E.-J. Cho, J. M. Ok, J. S. Kim, K. Kim, B. I. Min, H.-K. Lee, J.-Y. Kim, B.-G. Park, H.-D. Kim, and S. Lee, Sci. Rep. **4**, 3680 (2014).
[16] H. Takatsu, S. Yonezawa, S. Fujimoto, and Y. Maeno, Phys. Rev. Lett. **105**, 137201 (2010).

[17] H. Takatsu, G. Nénert, H. Kadowaki, H. Yoshizawa, M. Enderle, S. Yonezawa, Y. Maeno, J. Kim, N. Tsuji, M. Takata, Y. Zhao, M. Green, and C. Broholm, Phys. Rev. B **89**, 104408 (2014).
[18] H. Takatsu and Y. Maeno, J. Cryst. Growth **312**, 3461 (2010).
[19] G. E. Granroth, A. I. Kolesnikov, T. E. Sherline, J. P. Clancy, K. A. Ross, J. P. C. Ruff, B. D. Gaulin, and S. E. Nagler, J. Phys.: Conf. Ser. **251**, 012058 (2010).
[20] R. Bewley, J. Taylor, and S. Bennington., Nucl. Instr. Meth. Phys. Res. A **637**, 128 (2011).
[21] R. M. Ibberson, Nucl. Instr. Meth. Phys. Res. A **600**, 47 (2009).
[22] O. Arnold, J. Bilheux, J. Borreguero, A. Buts, S. Campbell, L. Chapon, M. Doucet, N. Draper, R. F. Leal, M. Gigg, V. Lynch, A. Markvardsen, D. Mikkelson, R. Mikkelson, R. Miller, K. Palmen, P. Parker, G. Passos, T. Perring, P. Peterson, S. Ren, M. Reuter, A. Savici, J. Taylor, R. Taylor, R. Tolchenov, W. Zhou, and J. Zikovsky, Nucl. Instr. Meth. Phys. Res. A **764**, 156 (2014).
[23] S. Toth and B. Lake, J. Phys.: Condens. Matter **27**, 166002 (2015).
[24] M. Rotter, J. Magn. Mag. Mat. **272**, E481 (2004).
[25] T. G. Perring, Ph.D. thesis, University of Cambridge, 1991.
[26] http://docs.mantidproject.org/interfaces/PyChop.html.
[27] A. C. Larson and R. B. V. Dreele, General Structure Analysis System (GSAS), Tech. Rep. (Los Alamos National Laboratory Report LAUR 86-748, 1994), http://11bm.xray.aps.anl.gov/downloads/gsas.
[28] B. H. Toby, J. Appl. Crystallogr. **34**, 210 (2001).
[29] T. Ozaki, Phys. Rev. B **67**, 155108 (2003).
[30] T. Ozaki and H. Kino, Phys. Rev. B **69**, 195113 (2004).
[31] M. J. Han, T. Ozaki, and J. Yu, Phys. Rev. B **73**, 045110 (2006).
[32] P. W. Stephens, J. Appl. Cryst. **32**, 281 (1999).
[33] T. Moriya, Phys. Rev. **120**, 91 (1960).
[34] H. Takatsu, H. Yoshizawa, S. Yonezawa, and Y. Maeno, Phys. Rev. B **79**, 104424 (2009).
[35] M. Poienar, F. Damay, C. Martin, J. Robert, and S. Petit, Phys. Rev. B **81**, 104411 (2010).
[36] M. Frontzek, J. T. Haraldsen, A. Podlesnyak, M. Matsuda, A. D. Christianson, R. S. Fishman, A. S. Sefat, Y. Qiu, J. R. D. Copley, S. Barilo, S. V. Shiryaev, and G. Ehlers, Phys. Rev. B **84**, 094448 (2011).
[37] L. Messio, C. Lhuillier, and G. Misguich, Phys. Rev. B **83**, 184401 (2011).
[38] L. Shekhtman, O. Entin-Wohlman, and A. Aharony, Phys. Rev. Lett. **69**, 836 (1992).
[39] W. Koshibae, Y. Ohta, and S. Maekawa, Phys. Rev. B **50**, 3767 (1994).
[40] M. Frontzek, G. Ehlers, A. Podlesnyak, H. Cao, M. Matsuda, O. Zaharko, N. Aliouane, S. Barilo, and S. V. Shiryaev, J. Phys.: Condens. Matter **24**, 016004 (2012).
[41] H. Kadowaki, H. Takei, and K. Motoya, J. Phys.: Condens. Matter **7**, 6869 (1995).
[42] A. Jain, S. P. Ong, G. Hautier, W. Chen, W. D. Richards, S. Dacek, S. Cholia, D. Gunter, D. Skinner, G. Ceder, and K. A. Persson, APL Mater. **1**, 011002 (2013).
[43] S. Tóth, B. Wehinger, K. Rolfs, T. Birol, U. Stuhr, H. Takatsu, K. Kimura, T. Kimura, H. M. Rønnow, and C. Rüegg, Nat. Commun. **7**, 13547 (2016).
[44] M.-T. Suzuki, T. Koretsune, M. Ochi, and R. Arita, Phys. Rev. B **95**, 094406 (2017).
[45] K. Park, J. Oh, J. C. Leiner, J. Jeong, K. C. Rule, M. D. Le, and J.-G. Park, Phys. Rev. B **94**, 104421 (2016).